# Geochemical Characteristics and U–Pb Dating of Granites in the Western Granitoid Belt of Thailand

Etsuo Uchida [1,*], Takumi Yokokura [1], Sota Niki [2] and Takafumi Hirata [2]

[1] Department of Resources and Environmental Engineering, Faculty of Science and Engineering, Waseda University, Ohkubo 3-4-1, Shinjuku, Tokyo 169-8555, Japan; tyokokura@toki.waseda.jp

[2] Geochemical Research Center, Graduate School of Science, The University of Tokyo, Hongo 7-3-1, Bunkyo, Tokyo 113-0064, Japan; niki@eqchem.s.u-tokyo.ac.jp (S.N.); hrt1@eqchem.s.u-tokyo.ac.jp (T.H.)

* Correspondence: weuchida@waseda.jp

**Abstract:** This paper presents the integration of magnetic susceptibility measurements and whole-rock geochemical compositional and Nd–Sr isotopic ratio analyses for granite samples collected from the Ranong, Lam Pi, Ban Lam Ru, and Phuket granite bodies in the Western Granitoid Belt of Thailand. In addition, U–Pb dating was performed on zircons extracted from the samples. All samples are proper granites based on their mineralogical and geochemical characteristics. Two samples collected from the Lam Pi granite body were classified as magnetite-series and I-type. The remaining granite samples were classified as ilmenite-series and S- or A-type. Furthermore, all granites were classified as syn-collision granites. Excluding the magnetite-series samples from the Lam Pi granite body, the other samples exhibit enrichment in incompatible elements, such as Nb, Sn, Ta, Pb, Bi, Th, U, Ce, Rb, and Cs. Zircon U–Pb dating yielded ages of ca. 60 Ma for the magnetite-series granites from the Lam Pi granite body, whereas ages of 88–84 Ma were obtained for the other granite bodies. Initial Nd–Sr isotopic ratios indicate a higher contribution of mantle material in the Lam Pi magnetite-series granites and a higher contribution of continental crust material in the other granites. Based on these compositional and zircon U–Pb age data, it is inferred that the 88–84 Ma granites formed as a result of the thickening of the continental crust owing to the collision between the Sibumasu and the West Burma blocks. In contrast, the ca. 60 Ma Lam Pi magnetite-series granites are thought to have been generated via partial melting of the mantle wedge associated with the subduction of the Neo-Tethyan oceanic crust beneath the West Burma Block.

**Keywords:** Western Granitoid Belt; Thailand; geochemical signature; Nd–Sr initial isotopic ratios; U–Pb dating; tectonic setting

## 1. Introduction

Southeast Asia consists of four blocks originating from the supercontinent of Gondwana, namely the South China, Indochina, Sibumasu, and West Burma Blocks (Figure 1), and the amalgamation of these blocks has resulted in the formation of many granitic rocks due to associated orogenic processes (e.g., [1,2]). This study aims to investigate the geochemical signatures and the formation age of granitic rocks in western Thailand near the boundary of the Sibumasu Block and the West Burma Block.

Granitic rocks in Thailand can be classified into the Eastern Granitoid Belt, the Central Granitoid Belt, and the Western Granitoid Belt [3]. In the present study, we report the results of magnetic susceptibility measurements, geochemical analyses, and U–Pb dating of zircons from the Ranong, Lam Pi, Ban Lam Ru, and Phuket granite bodies of the Western Granitoid Belt. In western Thailand and Malaysia, numerous tin (Sn) deposits are associated with granitic rocks, making it one of the world's leading suppliers of Sn (e.g., [4–8]), which occurs primarily as alluvial placer deposits [7]. The Western Granitoid Belt extends northward into Myanmar [8]. The present study also aims to investigate granites of the Western Granitoid

Belt to determine the tectonic setting in which the Sn-enriched granites were formed based on their geochemical characteristics and zircon U–Pb ages.

Eastern Thailand is part of the Indochina Block, whereas western Thailand belongs to the Sibumasu Block (Figure 1) [1,9–14]. The eastern part of the Indochina Block corresponds to the Loei Fold Belt and the Eastern Granitoid Belt. The Sukhothai Zone occupies the western part of the Indochina Block, and the Inthanon Suture Zone in the eastern part of the Sibumasu Block belongs to the Central Granitoid Belt. The western part of the Sibumasu Block is part of the Western Granitoid Belt. The boundary between the Indochina and Sibumasu blocks corresponds to the boundary between the Sukhothai and Inthanon Suture zones. The Paleo-Tethys Ocean separated the Indochina and Sibumasu blocks before their amalgamation. The West Burma Block lies to the west of the Sibumasu Block, and it is thought that the Meso-Tethys Ocean once separated the two blocks [3,15–18]. The Indian subcontinent was located to the west of the West Burma Block, separated by the Neo-Tethys Ocean. According to Gardiner et al. [8], the granitic rocks of the Western Granitoid Belt are thought to have formed in association with the subduction of the Neo-Tethyan oceanic crust beneath the West Burma and Sibumasu blocks. The Western Granitoid Belt of Thailand extends northward into the Mogok–Mandalay–Mergui Belt of Myanmar, where numerous granitic bodies are present.
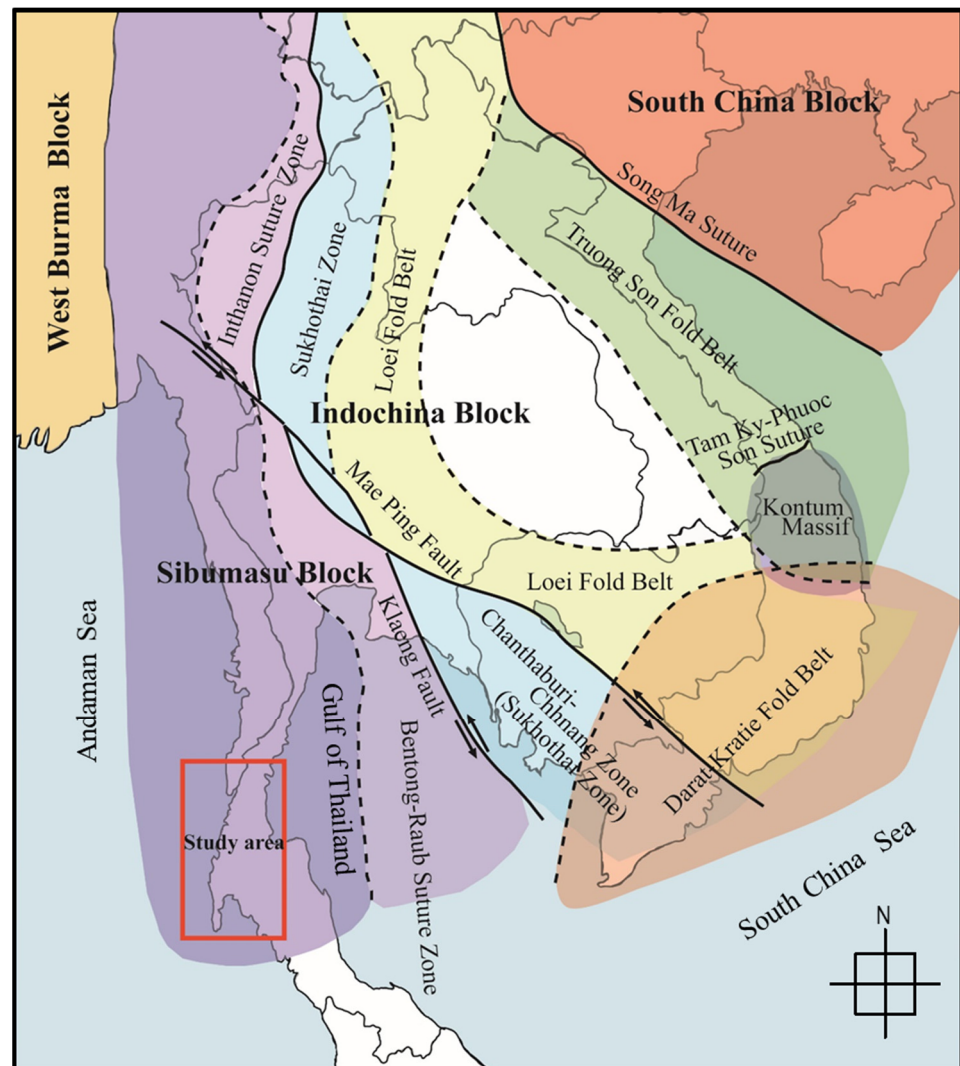
**Figure 1.** Tectonic subdivision of Southeast Asia [1,2,19–23]. The study area is indicated by the red rectangle.

## 2. Materials and Methods

Granite samples were collected from fifteen locations across the Phuket, Lam Pi, Ban Lam Ru, and Ranong granite bodies at sites 5, 5, 2, and 3, respectively (Figure 2) [24]. Latitude and longitude were measured at the sampling sites using GPS (eTrex Venture HC, Garmin Ltd., Schaffhausen, Switzerland). Magnetic susceptibility measurements were conducted at ten points surrounding each of the sampling sites using a portable magnetic susceptibility meter (SM30, ZM Instruments, Brno, Czech Republic). Measurements were conducted on smooth, fresh surfaces.
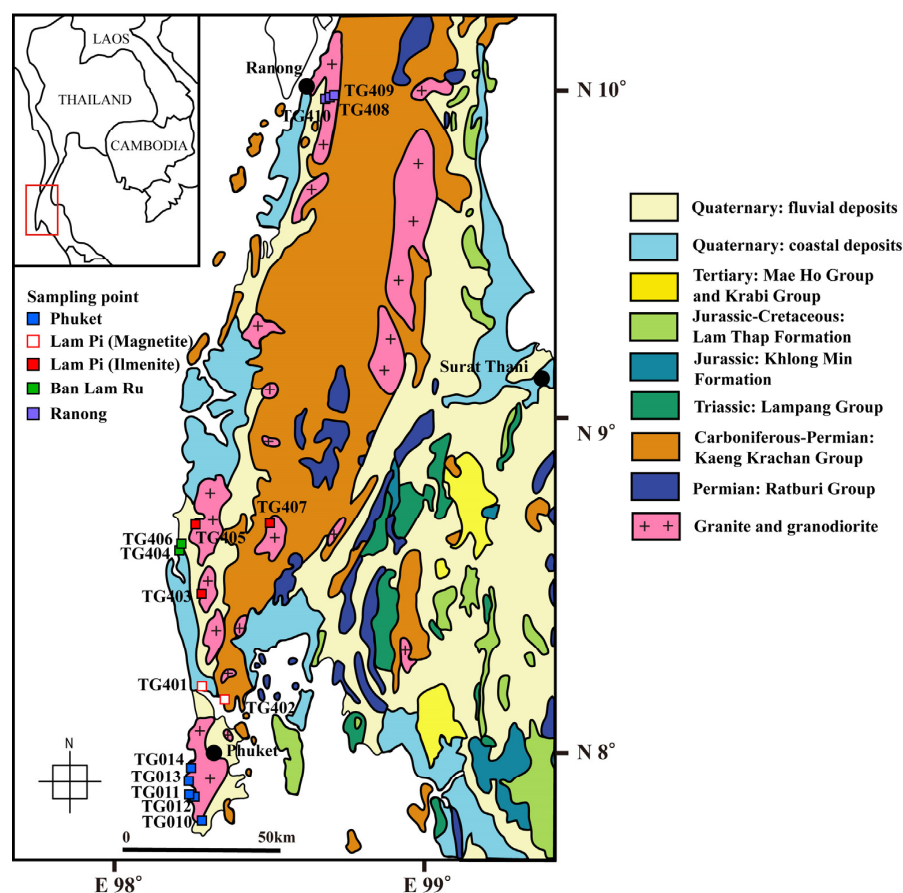
**Figure 2.** Geological map showing a distribution of the studied granites and sampling locations [24].

Thin sections were prepared from the collected samples, and the constituent minerals were identified using a polarizing microscope in transmitted light.

Samples were ground for one minute using a tungsten carbide vibrating mill (TI-100, Heiko Seisakusho, Fukushima, Japan) for whole-rock compositional analysis. After further grinding using an agate mortar, 5 g of each sample was sent to Activation Laboratories Ltd. (Ancaster, ON, Canada) for analysis of major and minor components based on the 5Litho package.

The chemical composition of biotite was determined using a scanning electron microscope (SEM; JSM-6360, JEOL, Tokyo, Japan) equipped with an energy-dispersive X-ray spectrometer (EDS; INCA Energy, Oxford Instruments, Abington, UK). Prior to analysis, sample surfaces were coated with carbon using a carbon coater (QUICK CARBON COATER SC-701C, Sanyu Denshi, Tokyo, Japan). The accelerating voltage was set at 15 kV, and the sample current was adjusted to achieve a total count rate of 2000 counts/s on a Co standard sample. The measurement time was set to 60 s. Analysis was conducted for Si, Ti, Al, Fe, Mg, Mn, Na, and K. Synthetic oxides were used as the standards for Si, Ti, Al, Fe, Mg, and Mn. Natural albite and orthoclase were utilized as standard samples for Na and K,

respectively. Prior to analysis, observations were made under a polarizing microscope, and measurements were conducted on fresh, unaltered minerals.

Zircon grains were separated from the granite samples for U–Pb dating using laser ablation–inductively coupled plasma–mass spectrometry (LA–ICP–MS). Samples were crushed in an iron mortar and sieved to a particle size of <250 μm. Then, light minerals were removed by panning in water. After drying, magnetic minerals were removed using a neodymium magnet. Subsequently, a density-adjusted sodium polytungstate solution with 3.0 g/cm$^3$ was used for centrifugation. Heavy particles that settled at the bottom of the container were extracted and deposited in a beaker using a pipette and washed thoroughly with distilled water to remove excess heavy liquid. Magnetic separation using a neodymium magnet was performed again after drying. Zircon grains were handpicked from the heavy fractions using a stereomicroscope and embedded on a glass slide with a thin coating of Petropoxy 154 resin (Burnham Petrographics LLC., Rathdrum, ID, USA) then heat-cured. Next, the zircons were polished using diamond paste in preparation for U–Pb dating. To identify suitable locations for spot analyses, cathodoluminescence images were captured using a field emission scanning electron microscope (FE-SEM; JSM-7001F, JEOL, Tokyo, Japan) equipped with a cathodoluminescence detector (MonoCL3 detector, Gatan, CA, USA) installed at the Kagami Memorial Research Institute for Materials Science and Technology of Waseda University (Tokyo, Japan).

Zircon U–Pb dating was conducted using the LA–ICP–MS facility installed at the Geochemical Research Center of the Graduate School of Science, The University of Tokyo (Tokyo, Japan). To remove contaminants from the surfaces of zircon grains, pre-ablation of each grain surface was performed using a femtosecond laser ablation system over a 40 μm square (Cyber Probe UV Plus, Cyber Laser Inc., Tokyo, Japan). The irradiation conditions for pre-ablation were set to a single repetition with a laser output of 30 mW. Subsequently, a laser with a beam diameter of 10 μm was directed at the center of the pre-ablated area. During measurements, the laser output was set at 30 mW, and a burst of 40 shots was applied. The vaporized samples from laser ablation were introduced into a multi-collector (MC)–ICP–MS (Nu Plasma 2, Nu Instruments, Wrexham, UK) using a mixture of He and Ar with a 0.6 L/min flow rate. The signal intensities of $^{206}$Pb, $^{207}$Pb, and $^{235}$U were detected using Daly ion detectors, and the signal intensities of $^{202}$Hg, $^{204}$(Hg + Pb), and $^{208}$Pb were detected using high-gain ion detectors. The signal intensity of $^{232}$Th was detected using a Faraday cup. For the signal intensity of $^{204}$Pb, it was assumed that $^{204}$Pb$_{blank}$ could be neglected, and the following equation was used:

$$^{204}\text{Pb} = {}^{204}(\text{Hg} + \text{Pb}) - {}^{202}\text{Hg} \times \left( \frac{{}^{204}(\text{Hg} + \text{Pb})}{{}^{202}\text{Hg}} \right)_{\text{blank}} \tag{1}$$

The detection of $^{235}$U employed the following equation [25]:

$$^{235}\text{U} = {}^{238}\text{U} \times \frac{1}{137.88} \tag{2}$$

Calibration of the high-gain ion detectors utilized the glass reference material NIST SRM612, which has an isotopic ratio of $^{207}$Pb/$^{206}$Pb = 0.9073 [26]. Calibration of the $^{206}$Pb/$^{238}$U ratio employed the primary standard Nancy 91,500 zircon, with $^{206}$Pb/$^{238}$U = 0.17928 ± 0.00018 and $^{207}$Pb/$^{206}$Pb = 0.07556 ± 0.00032 [27]. The GJ-1 zircon with a $^{206}$Pb/$^{238}$U age of 600.4 Ma [28] and the OD-3 zircon with a $^{206}$Pb/$^{238}$U age of 33.0 Ma [29] were used as secondary standards. During one measurement cycle, the NIST SRM612 standard sample was measured three times, the 91,500 zircon was measured three times, the GJ-1 zircon was measured once, and the unknown sample was measured up to 13 times. Then, the NIST SRM612 standard sample was measured three times again, followed by another three measurements of the 91,500 zircon.

IsoplotR was used to generate the Wetherill diagrams for the concordant or discordant (TG404) zircon samples [30], which were used to determine U–Pb ages. A zircon grain is

considered concordant if its 95% confidence error ellipse ($\pm 2\sigma$) intersects with the concordia curve. The concordia ages were computed by employing two-dimensional weighted means of the $^{207}Pb/^{235}U$ and $^{206}Pb/^{238}U$ ratios [31].

To determine Sr and Nd isotopic ratios, crushed samples were completely decomposed using a mixed acid ($HF$–$HNO_3$–$HClO_4$), followed by separation of Sr and Nd using columns packed with Sr and Ln resins (Eichrom Technologies Inc., University Lane Lisle, IL, USA), respectively. The samples were adjusted to ~100 ppb in 1% $HNO_3$ for Sr and Nd. The isotopic ratios of $^{87}Sr/^{86}Sr$ and $^{143}Nd/^{144}Nd$ were measured using MC–ICP–MS (Neptune, Thermo Fisher Scientific Ltd., Waltham, MA, USA) installed at the Research Institute for Humanity and Nature (Kyoto, Japan). The $^{87}Sr/^{86}Sr$ and $^{143}Nd/^{144}Nd$ ratios were corrected for mass fractionation effects during measurement using stable isotopic ratios in nature, with $^{86}Sr/^{88}Sr = 0.1194$ and $^{146}Nd/^{144}Nd = 0.7219$, respectively. Simultaneously measured values for the Sr standard sample NIST SRM 987 yielded an $^{87}Sr/^{86}Sr$ value of $0.710329 \pm 0.000032$ ($2\sigma$; n = 10), and those for the Nd standard sample JNdi-1 yielded a $^{143}Nd/^{144}Nd$ value of $0.512048 \pm 0.000022$ ($2\sigma$; n = 6). The obtained values were corrected to match the recommended values for the standard samples, which are $^{143}Nd/^{144}Nd = 0.512115$ [32] and $^{87}Sr/^{86}Sr = 0.710250$ [33], respectively. For further details regarding sample adjustment and measurement, please refer to Uchida et al. [34].

## 3. Results

### 3.1. Sample Descriptions

Figure 3 shows photographs of typical rock samples and their photomicrographs taken under a polarizing microscope. None of the samples showed linear structures. Each sample consists mainly of coarse- to medium-grained quartz, potassium feldspar, plagioclase, and biotite (Table 1). Hornblende is observed in samples TG010 from the Phuket granite body and TG401 from the Lam Pi granite body, whereas muscovite is observed in samples TG403-TG404 from the Lam Pi granite body and TG408-TG410 from the Ranong granite body. The accessory minerals include zircon, apatite, and tourmaline, and samples containing hornblende also contain minor titanite.

**Table 1.** Modal composition of the analyzed granite samples.

| Granite Body | Sample No. | Rock Type | Qz | Pl | Kfs | Bt | Hlb | Zrn | Ap | Ms | Ttn | Op | Cpx | Tur | Remarks |
|---|---|---|---|---|---|---|---|---|---|---|---|---|---|---|---|
| Phuket | TG010 | Hornblende-biotite granite | ○ | ○ | ○ | ○ | ○ | - | - | | △ | - | | | |
| | TG011 | Biotite granite | ◎ | ○ | ○ | ○ | | | | - | | | | | |
| | TG012 | Biotite granite | ◎ | ○ | ○ | ○ | | - | - | | | - | | △ | Plagioclase is partly altered. |
| | TG013 | Biotite granite | ◎ | ○ | ○ | ○ | | - | | ○ | | - | | - | |
| | TG014 | Biotite granite | ◎ | ○ | ○ | ○ | | - | - | | | - | | | Biotite is partly altered. |
| Lam Pi (Magnetite) | TG401 | Hornblende-biotite granite | ◎ | ◎ | ◎ | ○ | ○ | | | | △ | △ | | | Biotite and plagioclase are partly altered. |
| | TG402 | Biotite granite | ◎ | ◎ | ◎ | ○ | | - | - | | | | | | Biotite and plagioclase are partly altered. |
| Lam Pi (Ilmenite) | TG403 | Biotite granite | ◎ | ○ | ◎ | ○ | | - | - | ○ | | | | | Biotite and K-feldspar is partly altered. |
| | TG405 | Biotite granite | ◎ | ○ | ◎ | - | | | | ○ | | | | △ | Plagioclase is partly altered. |
| | TG407 | Biotite granite | ◎ | ○ | ◎ | - | | | | ○ | | | | △ | Plagioclase is partly altered. |

**Table 1.** *Cont.*

| Granite Body | Sample No. | Rock Type | Qz | Pl | Kfs | Bt | Hlb | Zrn | Ap | Ms | Ttn | Op | Cpx | Tur | Remarks |
|---|---|---|---|---|---|---|---|---|---|---|---|---|---|---|---|
| Ban Lam Ru | TG404 | Biotite granite | ◎ | ○ | ◎ | ◎ | | - | - | | | - | | | Biotite is partly altered. |
| | TG406 | Biotite granite | ◎ | ○ | ◎ | ◎ | | - | - | | | - | | - | Biotite is partly altered. |
| Ranong | TG408 | Biotite granite | ◎ | ○ | ◎ | ○ | | - | - | ○ | | | | △ | |
| | TG409 | Biotite granite | ○ | ○ | ○ | | | - | - | ○ | | | | | Biotite is altered. |
| | TG410 | Biotite granite | ○ | ○ | ◎ | ○ | | - | - | △ | | - | | - | Biotite is partly altered. |

Modal proportions: ◎, 50–30 vol%; ○, 30–10 vol%; △, 10–2 vol%; −, <2 vol%. Abbreviations: Qz, quartz; Pl, plagioclase; Kfs, K-feldspar; Bt, biotite; Hlb, hornblende; Zrn, zircon; Ap, apatite; Ms, muscovite; Ttn, titanite; Op, opaque minerals; Cpx, clinopyroxene; Tur, tourmaline.
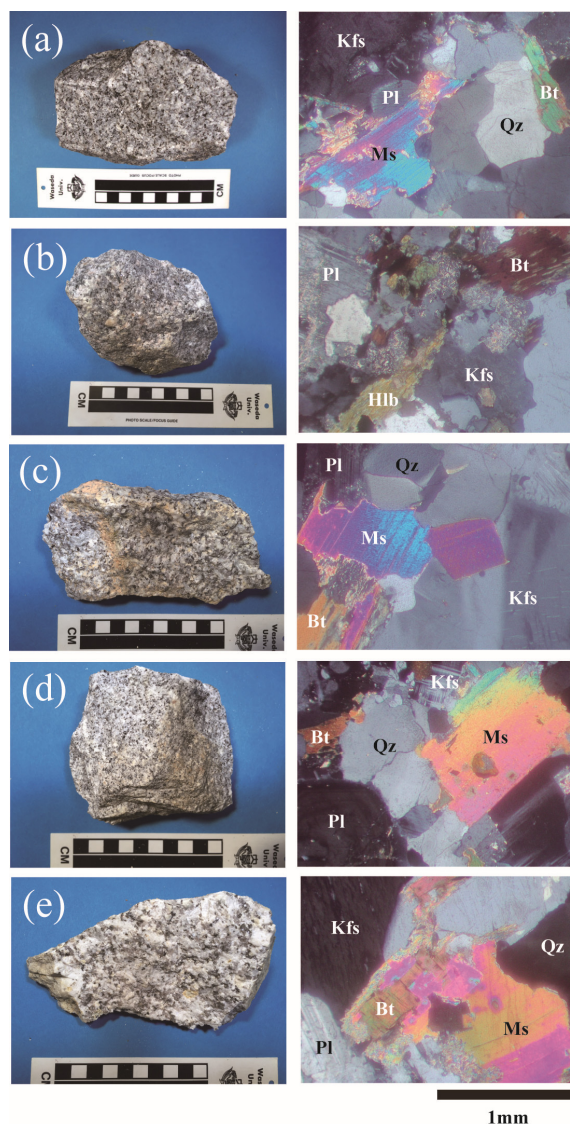
**Figure 3.** Photographs (**left**) and photomicrographs (**right**) taken using a polarizing microscope under crossed-polars showing representative granite samples: (**a**) TG013 from the Phuket granite body, (**b**) TG401 from the magnetite-series Lam Pi granite body, (**c**) TG405 from the Lam Pi ilmenite-series granite body, (**d**) TG404 from the Ban Lam Ru granite body, and (**e**) TG408 from the Ranong granite body. Abbreviations: Pl, plagioclase; Kfs, potassium feldspar; Qz, quartz; Bt, biotite; Hlb, hornblende; Ms, muscovite.

### 3.2. Magnetic Susceptibility

Based on their magnetic susceptibilities, granitic rocks are classified as magnetite-series if their magnetic susceptibility is $>3 \times 10^{-3}$ SI units and ilmenite-series if it is lower [35]. This distinction is believed to arise from differences in oxidation–reduction states influenced by the presence of organic matter in the source rocks [36]. Ilmenite-series granitic rocks are believed to form under relatively reducing conditions owing to the reducing action of organic matter in their source rocks or entrained sedimentary rocks. Figure 4 shows the magnetic susceptibilities of the studied samples. Except for two samples (TG401 and TG402 from the Lam Pi granite body), the studied granites exhibit magnetic susceptibilities of $<0.1 \times 10^{-3}$ SI units, and therefore, they can be classified as ilmenite-series rocks. The two samples from the Lam Pi granite body have markedly higher magnetic susceptibility values, averaging $8 \times 10^{-3}$ SI units, indicating that they can be classified as magnetite-series. However, the Lam Pi magnetite-series granite samples are surrounded by ilmenite-series granite with lower magnetic susceptibility, indicating a transition from magnetite- to ilmenite-series granite.
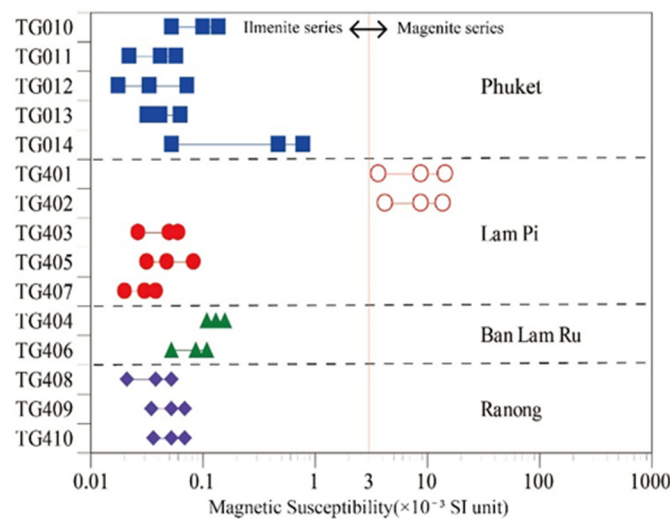
**Figure 4.** Magnetic susceptibilities (minimum, mean, and maximum values) at the granite sample locations.

### 3.3. Whole-Rock Geochemical Compositions

The results of whole-rock geochemical analysis are presented in Table 2.

**Table 2.** Results of whole-rock geochemical analysis of the studied granite samples.

| Location | | Phuket | | | | | Lam Pi | | | | Ban Lam Ru | | Ranong | | |
|---|---|---|---|---|---|---|---|---|---|---|---|---|---|---|---|
| Sample No. | | TG010 | TG011 | TG012 | TG013 | TG014 | TG401 | TG402 | TG403 | TG405 | TG407 | TG404 | TG406 | TG408 | TG409 | TG410 |
| SiO$_2$ | wt% | 67.96 | 73.38 | 72.88 | 73.79 | 72.56 | 67.81 | 70.33 | 70.65 | 72.03 | 73.03 | 71.12 | 72.05 | 74.48 | 74.21 | 72.00 |
| Al$_2$O$_3$ | wt% | 15.45 | 13.72 | 14.18 | 14.07 | 13.02 | 14.25 | 14.23 | 15.45 | 14.04 | 15.09 | 13.81 | 13.65 | 14.39 | 13.95 | 14.90 |
| Fe$_2$O$_3$ (T *) | wt% | 3.33 | 1.73 | 1.51 | 1.68 | 3.55 | 3.44 | 2.38 | 1.19 | 1.59 | 0.96 | 3.09 | 2.73 | 1.06 | 1.51 | 1.05 |
| MnO | wt% | 0.052 | 0.031 | 0.018 | 0.026 | 0.078 | 0.081 | 0.057 | 0.034 | 0.037 | 0.047 | 0.048 | 0.049 | 0.037 | 0.047 | 0.035 |
| MgO | wt% | 0.68 | 0.58 | 0.35 | 0.38 | 0.92 | 1.24 | 0.72 | 0.14 | 0.30 | 0.13 | 0.82 | 0.61 | 0.14 | 0.20 | 0.13 |
| CaO | wt% | 2.20 | 1.35 | 1.16 | 1.17 | 2.72 | 2.64 | 2.28 | 0.61 | 1.12 | 0.21 | 2.15 | 1.61 | 1.09 | 0.86 | 0.81 |
| Na$_2$O | wt% | 2.87 | 2.58 | 2.47 | 2.55 | 3.30 | 2.81 | 2.68 | 2.77 | 2.52 | 2.91 | 2.43 | 2.51 | 3.51 | 3.24 | 2.77 |
| K$_2$O | wt% | 6.27 | 5.41 | 6.10 | 6.02 | 2.09 | 4.38 | 4.95 | 7.87 | 5.90 | 5.92 | 5.31 | 5.71 | 4.45 | 5.09 | 7.41 |
| TiO$_2$ | wt% | 0.507 | 0.208 | 0.251 | 0.249 | 0.663 | 0.509 | 0.351 | 0.142 | 0.250 | 0.111 | 0.523 | 0.383 | 0.117 | 0.166 | 0.121 |
| P$_2$O$_5$ | wt% | 0.13 | 0.11 | 0.08 | 0.09 | 0.15 | 0.13 | 0.08 | 0.07 | 0.09 | 0.08 | 0.13 | 0.10 | 0.05 | 0.09 | 0.04 |
| LOI | wt% | 1.26 | 0.61 | 0.56 | 0.77 | 0.97 | 2.01 | 2.75 | 0.91 | 0.85 | 1.87 | 0.69 | 0.67 | 1.12 | 1.16 | 0.78 |
| Total | wt% | 100.7 | 99.71 | 99.57 | 100.8 | 100 | 99.29 | 100.8 | 99.83 | 98.75 | 100.4 | 100.1 | 100.1 | 100.5 | 100.5 | 100.1 |

**Table 2.** *Cont.*

| Location | | Phuket | | | | | Lam Pi | | | | Ban Lam Ru | | Ranong | | |
|---|---|---|---|---|---|---|---|---|---|---|---|---|---|---|---|---|
| Sample No. | | TG010 | TG011 | TG012 | TG013 | TG014 | TG401 | TG402 | TG403 | TG405 | TG407 | TG404 | TG406 | TG408 | TG409 | TG410 |
| Sc | ppm | 5 | 4 | 4 | 4 | 10 | 7 | 5 | 3 | 3 | 2 | 7 | 6 | 5 | 4 | 3 |
| Be | ppm | 7 | 13 | 11 | 7 | 15 | 4 | 6 | 8 | 8 | 10 | 8 | 11 | 11 | 9 | 9 |
| V | ppm | 24 | 18 | 15 | 13 | 36 | 65 | 40 | 6 | 10 | 6 | 27 | 20 | 6 | 6 | 6 |
| Ba | ppm | 586 | 219 | 258 | 224 | 170 | 566 | 458 | 226 | 192 | 78 | 347 | 257 | 57 | 98 | 300 |
| Sr | ppm | 145 | 53 | 62 | 57 | 85 | 320 | 251 | 46 | 44 | 22 | 95 | 68 | 24 | 33 | 56 |
| Y | ppm | 36 | 23 | 32 | 26 | 61 | 23 | 22 | 48 | 29 | 21 | 47 | 48 | 55 | 44 | 59 |
| Zr | ppm | 229 | 115 | 156 | 154 | 753 | 156 | 139 | 130 | 162 | 69 | 287 | 248 | 89 | 112 | 54 |
| Cr | ppm | <20 | <20 | <20 | <20 | <20 | <20 | <20 | <20 | <20 | <20 | 30 | <20 | <20 | <20 | <20 |
| Ni | ppm | <20 | <20 | <20 | <20 | <20 | <20 | <20 | <20 | <20 | <20 | <20 | <20 | 50 | <20 | <20 |
| Cu | ppm | <10 | <10 | <10 | <10 | 20 | <10 | <10 | <10 | 280 | 280 | 280 | <10 | <10 | 120 | 280 |
| Zn | ppm | 60 | 50 | 50 | 40 | 80 | 60 | 50 | 40 | 120 | 110 | 120 | 60 | 50 | 50 | 110 |
| Ga | ppm | 21 | 21 | 22 | 21 | 23 | 19 | 18 | 25 | 24 | 26 | 20 | 27 | 33 | 28 | 21 |
| Ge | ppm | 2 | 2 | 2 | 2 | 3 | 2 | 2 | 2 | 1 | 2 | 1 | 2 | 3 | 2 | 2 |
| As | ppm | <5 | <5 | <5 | <5 | 6 | <5 | <5 | <5 | <5 | <5 | <5 | <5 | 37 | <5 | <5 |
| Rb | ppm | 399 | 418 | 452 | 429 | 236 | 276 | 314 | 872 | 607 | 881 | 395 | 540 | 741 | 684 | 796 |
| Nb | ppm | 22 | 24 | 29 | 26 | 42 | 13 | 11 | 24 | 27 | 28 | 26 | 31 | 30 | 29 | 19 |
| Mo | ppm | <2 | <2 | <2 | <2 | <2 | <2 | <2 | <2 | <2 | <2 | <2 | <2 | <2 | <2 | <2 |
| Ag | ppm | 0.8 | <0.5 | 0.5 | <0.5 | 2.5 | <0.5 | <0.5 | <0.5 | 0.5 | <0.5 | 0.8 | 0.6 | <0.5 | <0.5 | <0.5 |
| In | ppm | <0.2 | <0.2 | <0.2 | <0.2 | <0.2 | <0.2 | <0.2 | 0.2 | 1.1 | 1.2 | 1 | 0.2 | 0.4 | 0.4 | 1.1 |
| Sn | ppm | 22 | 37 | 45 | 35 | 57 | 14 | 13 | 20 | 22 | 43 | 14 | 23 | 43 | 46 | 16 |
| Sb | ppm | <0.5 | <0.5 | <0.5 | <0.5 | <0.5 | <0.5 | <0.5 | <0.5 | 0.6 | 0.6 | 0.7 | <0.5 | <0.5 | <0.5 | <0.5 |
| Cs | ppm | 27.1 | 49.5 | 64 | 30.6 | 39.7 | 7.6 | 8.4 | 50.5 | 24.9 | 72.5 | 26.1 | 48.5 | 92.4 | 66.3 | 45.0 |
| La | ppm | 55.4 | 41.1 | 73.7 | 65 | 75.8 | 67.8 | 48.8 | 58.5 | 85.1 | 27.2 | 100 | 129 | 37.2 | 40.1 | 30.8 |
| Ce | ppm | 115 | 88.3 | 147 | 139 | 163 | 116 | 87.3 | 124 | 190 | 58.0 | 210 | 266 | 82.2 | 87.3 | 66.2 |
| Pr | ppm | 12.9 | 9.81 | 17.1 | 15.5 | 18.6 | 12.1 | 9.27 | 15.2 | 20.5 | 6.10 | 21.9 | 30.3 | 9.88 | 10.5 | 7.42 |
| Nd | ppm | 44.4 | 33.8 | 57.2 | 50.6 | 65.2 | 35.8 | 28.9 | 47.1 | 73.4 | 23.1 | 79.1 | 93.1 | 31.4 | 33.0 | 29.0 |
| Sm | ppm | 8.9 | 7.3 | 11.7 | 10.1 | 14.8 | 5.8 | 5.0 | 10.5 | 15.2 | 4.6 | 15.4 | 17.5 | 8.5 | 8.0 | 7.7 |
| Eu | ppm | 1.10 | 0.48 | 0.65 | 0.52 | 0.75 | 1.07 | 0.84 | 0.57 | 0.42 | 0.13 | 0.97 | 0.81 | 0.28 | 0.30 | 0.52 |
| Gd | ppm | 6.7 | 5.4 | 8.4 | 7.1 | 11.3 | 4.2 | 3.7 | 8.3 | 8.8 | 3.1 | 9.9 | 11.8 | 7.9 | 6.4 | 7.4 |
| Tb | ppm | 1.1 | 0.8 | 1.2 | 1.0 | 1.8 | 0.7 | 0.6 | 1.6 | 1.3 | 0.5 | 1.5 | 1.9 | 1.7 | 1.3 | 1.4 |
| Dy | ppm | 6.1 | 4.1 | 6.1 | 5.0 | 9.4 | 4.0 | 3.6 | 9.3 | 5.9 | 2.9 | 8.5 | 10.3 | 10.7 | 8.2 | 9.2 |
| Ho | ppm | 1.2 | 0.7 | 1.0 | 0.9 | 1.8 | 0.8 | 0.7 | 1.7 | 0.9 | 0.6 | 1.5 | 1.8 | 2.0 | 1.4 | 1.8 |
| Er | ppm | 3.2 | 1.9 | 2.6 | 2.2 | 5.3 | 2.2 | 2.0 | 4.6 | 2.3 | 1.5 | 4.4 | 4.9 | 5.9 | 4.0 | 5.4 |
| Tm | ppm | 0.45 | 0.25 | 0.35 | 0.29 | 0.83 | 0.35 | 0.31 | 0.65 | 0.28 | 0.22 | 0.61 | 0.70 | 0.92 | 0.62 | 0.82 |
| Yb | ppm | 3.0 | 1.6 | 2.3 | 1.8 | 5.9 | 2.4 | 2.1 | 4.0 | 1.7 | 1.4 | 3.9 | 4.4 | 6.3 | 4.1 | 5.3 |
| Lu | ppm | 0.49 | 0.25 | 0.36 | 0.29 | 1.06 | 0.41 | 0.35 | 0.59 | 0.27 | 0.23 | 0.60 | 0.63 | 0.99 | 0.6 | 0.83 |
| Hf | ppm | 5.8 | 3.3 | 4.4 | 4.3 | 21.8 | 4.7 | 4.1 | 4.3 | 4.8 | 2.1 | 7.5 | 8.4 | 4.1 | 4.3 | 3.4 |
| Ta | ppm | 3.4 | 5.5 | 5.8 | 4.4 | 6.0 | 2.0 | 2.0 | 7.2 | 8.9 | 8.2 | 3.7 | 6.2 | 12.2 | 9.0 | 4.8 |
| Tl | ppm | 2.4 | 2.3 | 2.7 | 2.3 | 1.6 | 1.3 | 1.6 | 5.1 | 2.4 | 4.3 | 1.2 | 3.1 | 4.3 | 4.3 | 4.0 |
| Pb | ppm | 72 | 55 | 69 | 51 | 32 | 27 | 30 | 104 | 86 | 71 | 76 | 81 | 79 | 64 | 139 |
| Bi | ppm | 2.6 | 2.1 | 1.1 | 2.4 | 2.4 | <0.4 | <0.4 | 2.5 | 1.6 | 3.1 | 1.2 | 2.3 | 2.8 | 4.5 | 3.1 |
| Th | ppm | 62.0 | 39.5 | 64.5 | 64.0 | 229 | 44.3 | 39.5 | 75.8 | 90.9 | 28.6 | 83.0 | 134 | 50.9 | 59.7 | 49.7 |
| U | ppm | 15.1 | 24.0 | 17.2 | 12.5 | 146 | 11.8 | 11.6 | 32.0 | 11.5 | 16.5 | 11.7 | 35.1 | 32.1 | 34.6 | 26.2 |

* Total iron as $Fe_2O_3$.

All samples plot in the granite field using the total alkali vs. $SiO_2$ (TAS) diagram (Figure 5). Furthermore, 11 samples belong to the alkaline series [37,38].

Excluding the Lam Pi granite samples (TG401 and TG402), which have high magnetic susceptibilities, the other studied samples are enriched in incompatible elements, such as Nb, Sn, Ta, Pb, Bi, Th, U, Ce, Rb, and Cs. In particular, the samples have high contents of Sn, with values ranging from 14 to 57 ppm. In comparison, the Lam Pi magnetite-series granite samples have relatively lower values of 13–14 ppm. The contents for U and Th are 11–35 ppm and 28–234 ppm, respectively, except for sample TG014, which shows higher values of 146 ppm and 229 ppm, respectively.

Most samples plot within the field for S-type granites on a $Na_2O$ vs. $K_2O$ diagram (Figure 6) [39]. However, on an $Al_2O_3/(Na_2O + K_2O)$ vs. $Al_2O_3/(CaO + Na_2O + K_2O)$ (A/NK vs. A/CNK) diagram (Figure 7), most samples have A/CNK molar ratios of 1.0–1.1, indicating that they are peraluminous, and most plot within the I-type granite domain [40].
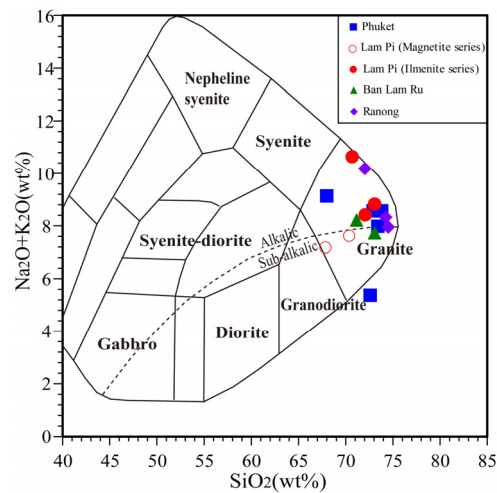
**Figure 5.** Diagram of $Na_2O$ + $K_2O$ vs. $SiO_2$ (TAS) for the studied granite samples [37,38]. The dividing line between the alkalic and sub-alkalic fields follows Irvine and Baragar [39].
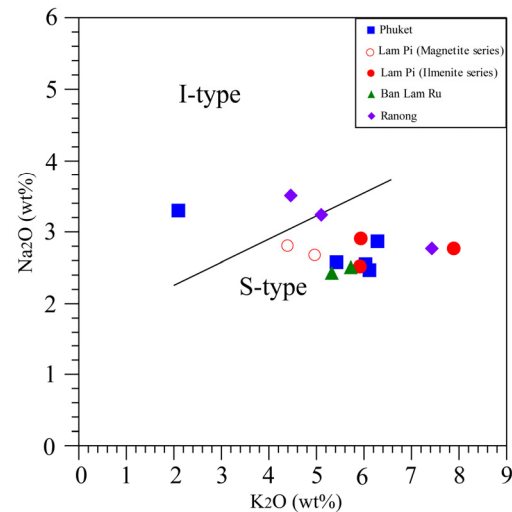
**Figure 6.** Diagram of $Na_2O$ vs. $K_2O$ showing the classification of the studied granite samples as I- and S-types [40].

In a Zr vs. 10,000 × Ga/Al diagram, the two samples from the Lam Pi granite body that are classified as magnetite-series are categorized as I&S-types, whereas most of the other samples, plot within the field for A-type granites (Figure 8).

On the Rb vs. (Yb + Ta) tectonic discrimination diagram, except for one sample (TG014) from the Phuket granite body, the studied samples plot within the field for syn-collision granite (Figure 9) [43]. Of these samples, TG401 and TG402 from the Lam Pi granite body plot closest to the volcanic arc granite field.

On the Sr/Y vs. Y diagram, the studied samples plot within the non-adakitic (calc-alkaline) field (Figure 10) [44]. However, samples TG401 and TG402 from the Lam Pi granite body exhibit slightly higher Sr/Y ratios compared with the other granite samples.

The chondrite-normalized [45] rare earth element patterns [45] of the samples exhibit markedly negative Eu anomalies (Figure 11). However, magnetite-series samples TG401 and TG402 from the Lam Pi granite body have smaller negative Eu anomalies compared with the other granite samples.
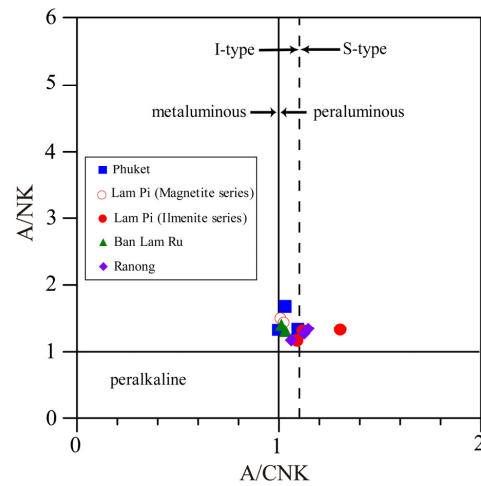
**Figure 7.** Diagram of $Al_2O_3/(Na_2O + K_2O)$ vs. $Al_2O_3/(CaO + Na_2O + K_2O)$ showing the classification of the studied samples as metaluminous and peraluminous, as well as I- and S-types [40,41].
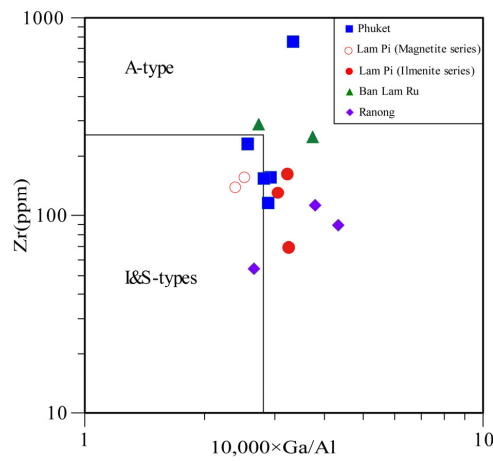
**Figure 8.** Diagram of Zr vs. $10{,}000 \times Ga/Al$ diagram showing the classification of the studied samples as I&S- and A-types [42].
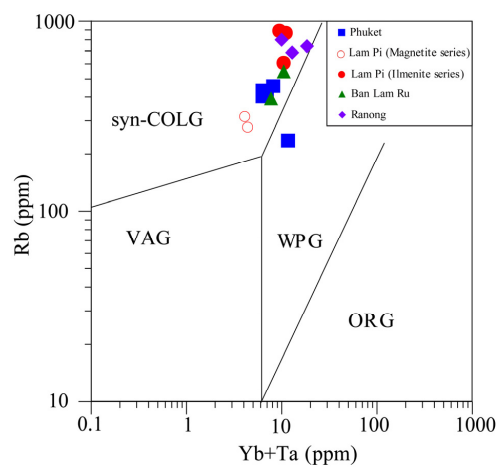
**Figure 9.** Tectonic setting discrimination diagram for the studied granite samples [43]. Abbreviations: syn-COLG, syn-collision granite; VAG, volcanic arc granite; WPG, within-plate granite; ORG, ocean-ridge granite.
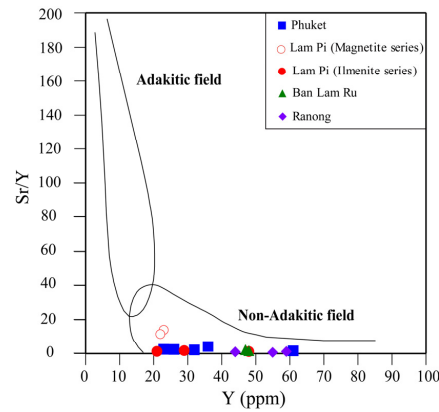
**Figure 10.** Sr/Y vs. Y diagram for the studied samples showing their classification as adakitic and non-adakitic rocks (calc-alkaline rocks) [44].
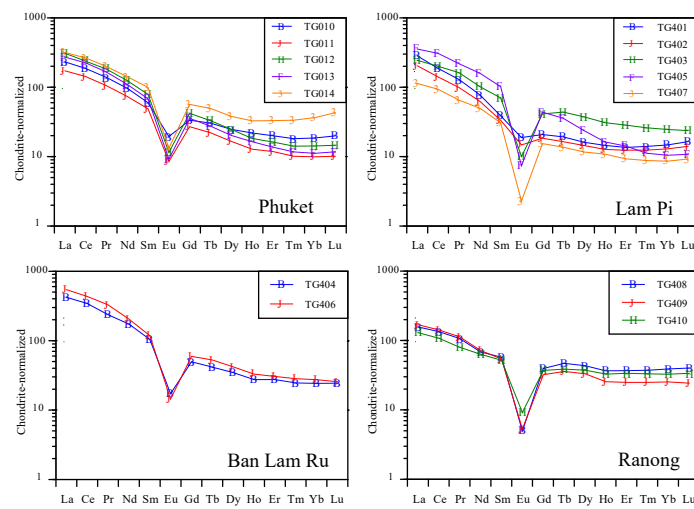
**Figure 11.** Chondrite-normalized rare-earth element patterns for the studied samples [45,46].

## 3.4. Chemistry of Biotite

The results of the chemical composition analysis of biotite are summarized in the Supplementary Materials (Table S1).

Figure 12 shows a plot of Mg/(Mg + Fe) vs. total Al for biotite from the studied samples based on O = 22. Overall, biotite with lower total Al tends to exhibit higher Mg/(Mg + Fe) molar ratios. Biotites from magnetite-series samples TG401 and TG402 from the Lam Pi granite body have the lowest total Al content and the highest Mg/(Mg + Fe) molar ratios of the studied samples.
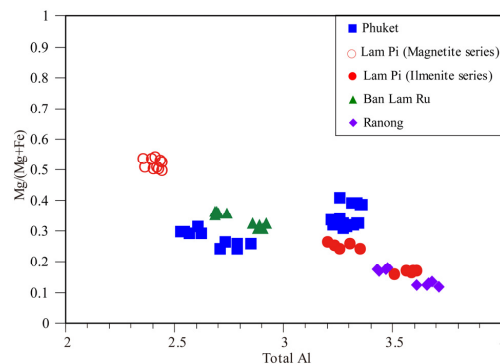
**Figure 12.** Diagram of Mg/(Mg + Fe) vs. total Al for biotite from the studied samples based on O = 22.

### 3.5. Zircon U–Pb Dating

Figure 13 shows representative cathodoluminescence images of the analyzed zircon grains. The results of zircon U–Pb dating analysis of the studied samples are shown in the Supplementary Materials (Table S2) and Figure 14 [30]. All ages fall within the range of 88–60 Ma, indicating that the granites formed during the Late Cretaceous to Early Paleogene.
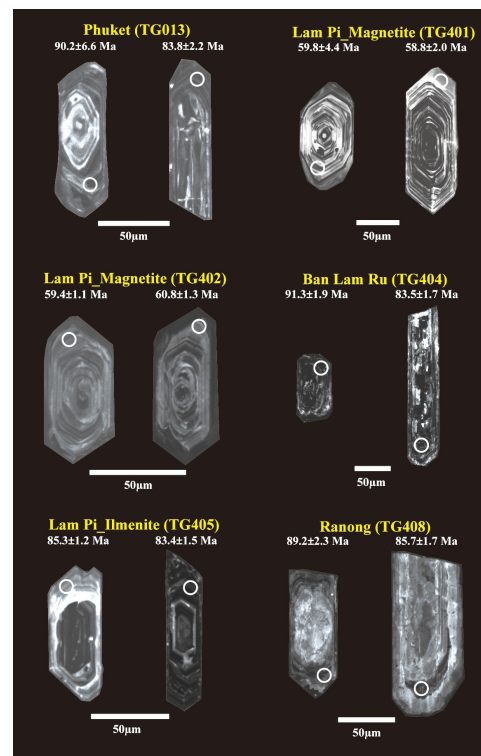
**Figure 13.** Cathodoluminescence images of representative zircons used for U–Pb dating. Open circles in the figure indicate measurement locations. Ages shown in the figure are based on $^{206}$Pb/$^{238}$U ratios.

### 3.6. Initial Nd and Sr Isotopic Ratios

The measured $^{143}$Nd/$^{144}$Nd and $^{87}$Sr/$^{86}$Sr isotopic ratios for the studied granite samples are presented in Table 3.

The initial $^{143}$Nd/$^{144}$Nd and $^{87}$Sr/$^{86}$Sr ratios calculated using the U–Pb ages derived from zircons in each granite body, as determined in Section 3.5, are shown in Table 3 and Figure 15 [33,47].

The initial $^{143}$Nd/$^{144}$Nd ratios range from 0.511741 to 0.512118, with negligible differences observed among the studied granite bodies. In contrast, the samples yield a wide range of initial $^{87}$Sr/$^{86}$Sr ratios from 0.709144 to 0.743762. Among the obtained results, samples TG401 and TG402 from the Lam Pi granite body yield low initial $^{87}$Sr/$^{86}$Sr ratios of 0.711563–0.712490, whereas the remaining samples yield relatively high values of 0.709144–0.743762.

**Table 3.** Nd–Sr isotopic ratios of the studied granite samples.

| Location | Sample No. | Age (Ma) | $^{87}$Sr/$^{86}$Sr | Std. Err. | ($^{87}$Sr/$^{86}$Sr)$_i$ | $^{143}$Nd/$^{144}$Nd | Std. Err. | ($^{143}$Nd/$^{144}$Nd)$_i$ |
|---|---|---|---|---|---|---|---|---|
| | TG010 | | 0.727991 | 0.000006 | 0.718703453 | 0.512032 | 0.000008 | 0.511962877 |
| | TG011 | | 0.770492 | 0.000006 | 0.743761515 | 0.511826 | 0.000009 | 0.511751607 |
| Phuket | TG012 | 84 | 0.766172 | 0.000010 | 0.741473653 | 0.511828 | 0.000007 | 0.511757048 |
| | TG013 | | 0.767556 | 0.000006 | 0.742054949 | 0.511849 | 0.000007 | 0.511779572 |
| | TG014 | | 0.750010 | 0.000005 | 0.740618899 | 0.511820 | 0.000006 | 0.511741243 |

| Location | Sample No. | Age (Ma) | $^{87}$Sr/$^{86}$Sr | Std. Err. | ($^{87}$Sr/$^{86}$Sr)$_i$ | $^{143}$Nd/$^{144}$Nd | Std. Err. | ($^{143}$Nd/$^{144}$Nd)$_i$ |
|---|---|---|---|---|---|---|---|---|
| Lam Pi (Magnetite) | TG401 | 60 | 0.713640 | 0.000007 | 0.71156355 | 0.512158 | 0.000008 | 0.512118283 |
| | TG402 | | 0.715502 | 0.000005 | 0.712489884 | 0.512107 | 0.000009 | 0.512064296 |
| Lam Pi (Ilmenite) | TG403 | 84 | 0.791899 | 0.000007 | 0.727515323 | 0.511888 | 0.000013 | 0.511810696 |
| | TG405 | | 0.774418 | 0.000006 | 0.727643868 | 0.511898 | 0.000008 | 0.511830054 |
| | TG407 | | 0.863871 | 0.000006 | 0.726903984 | 0.511902 | 0.000007 | 0.511769613 |
| Ban Lam Ru | TG404 | 86 | 0.743643 | 0.000008 | 0.729252537 | 0.511929 | 0.000009 | 0.511828501 |
| | TG406 | | 0.750828 | 0.000009 | 0.723325131 | 0.511839 | 0.000006 | 0.511862118 |
| Ranong | TG408 | 88 | 0.819298 | 0.000006 | 0.709143712 | 0.511942 | 0.000009 | 0.511843251 |
| | TG409 | | 0.799913 | 0.000006 | 0.726103382 | 0.512113 | 0.000011 | 0.5120252 |
| | TG410 | | 0.774152 | 0.000005 | 0.723662595 | 0.511926 | 0.000008 | 0.511829181 |
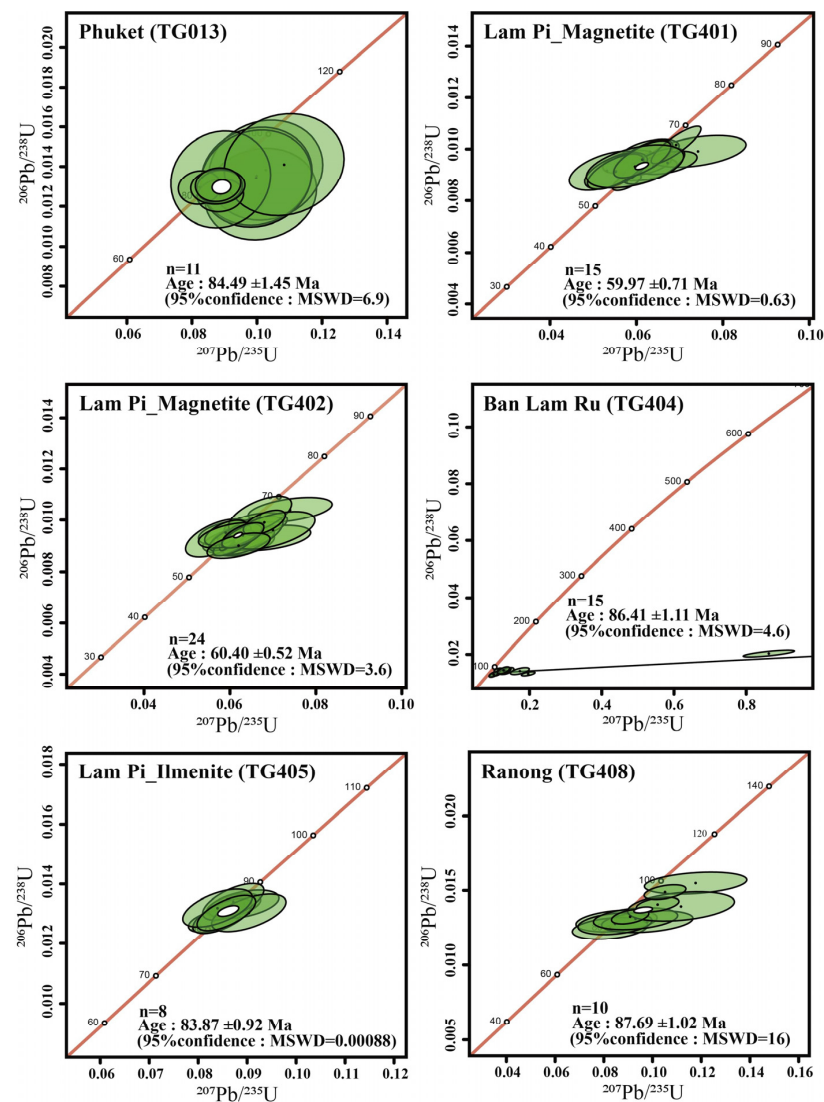
**Figure 14.** Wetherill diagrams showing the results of U–Pb dating of zircons from the studied granite samples [30].
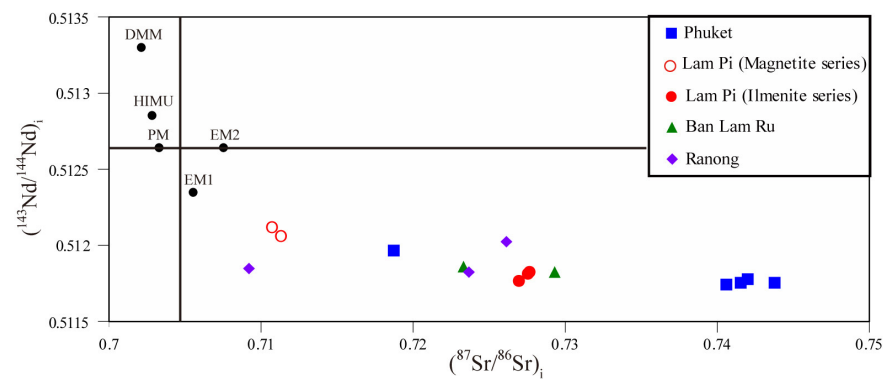
**Figure 15.** Initial $^{143}$Nd/$^{144}$Nd and $^{87}$Sr/$^{86}$Sr ratios of the studied granite samples. Abbreviations: PM, primitive mantle; CHUR, chondritic uniform reservoir; DMM, depleted MORB mantle; EM1, enriched mantle 1; EM2, enriched mantle 2; HIMU, high μ. PM, CHUR, DMM, EM1, EM2, and HIMU data are from Faure and Mensing [33] and Schaefer [46].

## 4. Discussion

The studied granite samples from the Phuket, Lam Pi, Ban Lam Ru, and Ranong granite bodies in the Western Granitoid Belt of Thailand tend to have high SiO$_2$ and Na$_2$O + K$_2$O contents and are classified as granites in a TAS diagram (Figure 5). Furthermore, most of the samples belong to the alkalic series. Magnetic susceptibility measurements classified samples TG401 and TG402 from the Lam Pi granite body as magnetite-series, whereas the remaining samples were classified as ilmenite-series (Figure 4). Based on Na$_2$O vs. K$_2$O contents, most of the samples can be classified as S-type granites, except for sample TG104 from the Phuket granite body and sample TG408 from the Ranong granite body, which are classified as I-type granites (Figure 6). However, the A/CNK molar ratios of the samples indicate that two of the samples (TG014 and TG408) are S-type granites, whereas the others are peraluminous I-type granites (Figure 7), which is inconsistent with the classification based on Na$_2$O vs. K$_2$O contents. Furthermore, the classification of the samples into I&S- and A-types using a Zr vs. 10,000 × Ga/Al diagram indicates that most of the samples are A-type granites (Figure 8).

The Lam Pi magnetite-series granites are surrounded by ilmenite-series granites, indicating that the Lam Pi magnetite-series granites intruded older ilmenite-series granites. Except for the magnetite-series samples TG401 and TG402 from the Lam Pi granite body, the other granite samples exhibit enrichment in incompatible elements such as Nb, Sn, Ta, Pb, Bi, Th, U, Ce, Rb, and Cs. In particular, the samples have high contents of Sn (14–57 ppm) (Table 2). Apart from these two samples from the Lam Pi granite body, the rare-earth elements (REE) patterns of the studied samples exhibit markedly negative Eu anomalies (Figure 11), consistent with plagioclase fractionation under reducing conditions. Accordingly, it is suggested that such fractionation processes led to the enrichment of incompatible elements, including Sn. In terms of biotite geochemical compositions within the granite bodies, samples TG401 and TG402 from the Lam Pi granite body have notably higher Mg/(Mg + Fe) ratios and lower total Al contents compared with the other studied samples (Figure 12). The above results for biotite geochemical composition are consistent with trends observed in Japanese and South Korean granitic rocks [48,49]. In addition, the initial Sr isotopic ratios of the Lam Pi magnetite-series granite samples are lower, indicating a substantial influence from mantle material. Conversely, except for sample TG408 from the Ranong granite body, the initial Sr isotopic ratios of the other ilmenite-series samples are high, suggesting derivation from continental crust material (Figure 15).

The results of zircon U–Pb dating indicate that the ilmenite-series granite bodies were emplaced during the Late Cretaceous (88–84 Ma) (Figure 14). In contrast, younger ages of ca. 60 Ma were obtained for the magnetite-series granite samples TG401 and TG402 from the Lam Pi granite body. The zircon ages obtained during this study are consistent with the $^{40}$Ar/$^{39}$Ar ages of 80–50 Ma reported by Charusiri et al. [1].

The Wuntho–Popa Arc, which is part of the West Burma Block, is located to the west of the Western Granitoid Belt in Thailand (Figure 1) and its northern extension, i.e., the Mogok–Mandaley–Mergui Belt in Myanmar. In contrast to the Western Granitoid Belt and the Mogok–Mandaley–Mergui Belt, the Wuntho–Popa Arc contains I-type granites and hosts mineral deposits such as gold, copper, and molybdenum [8,12]. It has been reported that the collision between the West Burma and Sibumasu blocks occurred during the Late Cretaceous [50]. The ilmenite-series and S- or A-type granites distributed in the Western Granitoid Belt are believed to have formed as a result of the collision between the West Burma and Sibumasu blocks at 88–84 Ma, followed by the subduction of the Neo-Tethyan oceanic crust beneath the West Burma and Sibumasu blocks at ca. 60 Ma, leading to the formation of magnetite-series granites (e.g., [51,52]) (Figure 16). Based on Rb vs. (Yb + Ta) tectonic discrimination diagram, it is inferred that the ilmenite-series and S- or A-type granites of the Western Granitoid Belt of Thailand formed in response to the collision between the West Burma and Sibumasu blocks (Figure 9). This collision resulted in the thickening of the continental crust at the western margin of the Sibumasu Block [53,54], leading to the formation of ilmenite-series and S- or A-type granites (Figure 16). The high initial Sr isotopic ratios of these S- or A-type granites indicate that they were derived via partial melting of continental crust material (Figure 15). Furthermore, advanced crystal differentiation processes led to the enrichment of incompatible elements, such as Sn, in the magma that formed the granites. In contrast, it is deduced that the formation of the Lam Pi magnetite-series granites in the Western Granitoid Belt have been associated with the subduction of the Neo-Tethyan oceanic crust, which was located west of the West Burma Blocks. Gardinier et al. [8] reported the occurrence of substantial Sn mineralization in parts of the Andes Mountains of South America that are far from the subduction zones of the Pacific Plate. In contrast, porphyry Cu–Au deposits in the Andes Mountains occur closer to the subduction zones. This relationship is likened to the relationship between the Wuntho–Popa Arc and the Mogok–Mandalay–Mergui and Western Granitoid belts. However, it is difficult to compare the distributions of different deposit types in the Andes Mountains with the mineralization in the Wuntho–Popa Arc and the Mogok–Mandalay–Mergui and Western Granitoid belts because the mineralization in these regions does not occur on the same continental block, as is the case in the Andes Mountains.
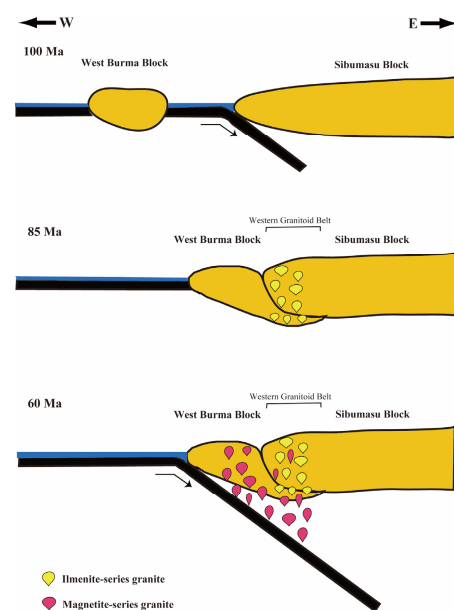
**Figure 16.** Schematic diagram showing the tectonic evolution and granite formation between the Sibumasu and West Burma blocks.

## 5. Conclusions

(1) Based on mineralogical and geochemical characteristics, granitic rock samples collected from the Ranong, Lam Pi, Ban Lam Ru, and Phuket granitic bodies of the Western Granitoid Belt, Thailand, can all be classified strictly as granites. Two samples collected from the Lam Pi granite body are magnetite-series and I-type, whereas the rest of the samples are ilmenite-series and S- or A-type.

(2) Initial Sr isotopic ratios suggest that the magnetite-series granites from the Lam Pi granite body contain a significant contribution from mantle material, whereas the other granites predominantly reflect derivation from continental crust.

(3) The granite bodies, except for the magnetite-series granite of the Lam Pi granite body, yield ages of 88–84 Ma, indicating that they formed during the thickening of the continental crust that occurred in response to the collision between the Sibumasu and West Burma blocks.

(4) The magnetite-series granite of the Lam Pi granite body yields an age of ca. 60 Ma and is believed to have formed in response to the subduction of the Neo-Tethyan oceanic crust beneath the West Burma and Sibumasu blocks.

(5) It is speculated that during the collision between the Sibumasu and West Burma blocks, advanced crystal differentiation of the granite magma led to the formation of granites enriched in incompatible elements such as Sn.

**Supplementary Materials:** The following supporting information can be downloaded at: https://www.mdpi.com/article/10.3390/geosciences14050135/s1, Table S1. Chemical composition of biotite by SEM-EDS; Table S2. Results of zircon U–Pb dating.

**Author Contributions:** Conceptualization, E.U.; methodology, E.U., T.Y., S.N. and T.H.; formal analysis, E.U., T.Y. and S.N.; investigation, E.U. and T.Y; resources, E.U. and T.Y.; data curation, E.U., T.Y. and S.N.; writing—original draft preparation, E.U.; writing—reviewing and editing, E.U. and T.Y.; visualization, E.U. and T.Y.; supervision, E.U.; project administration, E.U.; funding acquisition, E.U. and T.H. All authors have read and agreed to the published version of the manuscript.

**Funding:** This research was supported by a funding from the Japan Society for the Promotion of Science (Nos 16K06931 (E.U.), 19K05356 (E.U.), and A2624709 (T.H.)) and by a Waseda University Grant for Special Research Projects (2022R-015).

**Data Availability Statement:** All data are included/referenced in this article.

**Acknowledgments:** This research was conducted in part with the support of the Joint Research Grant for the Environmental Isotope Study of Research Institute for Humanity and Nature. The authors express their gratitude to three anonymous reviewers for their useful comments and suggestions that improve the quality of the manuscript. We thank Edanz for editing a draft of this manuscript.

**Conflicts of Interest:** The authors declare no conflicts of interest.

## References

1. Metcalfe, I. Gondwana dispersion and Asian accretion: Tectonic and palaeogeographic evolution of eastern Tethys. *J. Asian Earth Sci.* **2013**, *66*, 1–33. [CrossRef]
2. Wang, Y.; He, H.; Cawood, P.A.; Srithai, B.; Feng, Q.; Fan, W.; Zhang, Y.; Qiana, X. Geochronological, elemental and Sr-Nd-Hf-O isotopic constrains on the petrogenesis of the Triassic post-collisional granitic rocks in NW Thailand and its Paleotethyan implications. *Lithos* **2016**, *266*, 264–286. [CrossRef]
3. Charusiri, P.; Clark, A.H.; Farrad, E.; Archibald, D.; Charusiri, B. Granite belts in Thailand: Evidence from the $^{40}$Ar/$^{39}$Ar geochronological and geological syntheses. *J. SE Asian Earth Sci.* **1993**, *8*, 127–136. [CrossRef]
4. Hutchison, C.S.; Taylor, D. Metallogenesis in SE Asia. *J. Geol. Soc. Lond.* **1978**, *135*, 407–428. [CrossRef]
5. Ishihara, S.; Sawata, H.; Shibata, K.; Terashima, S.; Arrykul, S.; Sato, K. Granites and Sn-W deposits of Peninsular Thailand. In *Granitic Magma and Related Mineralization*; Ishihara, S., Takenouchi, S., Eds.; Min. Geol. Spec. Issue; Society of Mining Geologists of Japan: Tokyo, Japan, 1980; Volume 8, pp. 223–241.
6. Cobbing, E.J.; Mallick, D.I.J.; Pitfield, P.E.J.; Teoh, L.H. The granites of the Southeast Asia Tin Belt. *J. Geol. Soc. Lond.* **1986**, *143*, 537–550. [CrossRef]
7. Zaw, K. Geological, petrological and geochemical characteristics of granitoid rocks in Burma: With special reference to the associated W–Sn mineralization and their tectonic setting. *J. SE Asian Earth Sci.* **1990**, *4*, 293–335. [CrossRef]

8. Gardiner, N.J.; Searle, M.P.; Robb, L.J.; Morley, C.K. Neo-Tethyan magmatism and metallogeny in Myanmar—An Andean analogue? *J. Asian Earth Sci.* **2015**, *106*, 197–215. [CrossRef]

9. Searle, M.P.; Whitehouse, M.J.; Robb, L.J.; Ghani, A.A.; Hutchison, C.S.; Sone, M.; Ng, S.W.P.; Roselee, M.H.; Chung, S.L.; Oliver, G.J.H. Tectonic evolution of the Sibumasu Indochina terrane collision zone in Thailand and Malaysia: Constraints from new U-Pb zircon chronology of SE Asian tin granitoids. *J. Geol. Soc.* **2012**, *169*, 489–500. [CrossRef]

10. Pollard, P.J.; Nakapadungrat, S.; Taylor, R.G. The Phuket Supersuite, Southwest Thailand: Fractionated I-type granites associated with tin-tantalum mineralization. *Econ. Geol.* **1995**, *90*, 586–602. [CrossRef]

11. Hara, H.; Wakkita, K.; Ueno, K.; Kamata, Y.; Hisada, K.; Charusiri, P.; Charoentitirat, T.; Chaodumrong, P. Nature of accretion related to Paleo-Tethys subduction recorded in northern Thailand: Constrains from mélange kinematics and illite crystallinity. *Gondowana Res.* **2009**, *16*, 310–320. [CrossRef]

12. Burrett, C.; Zaw, K.; Meffre, S.; Lai, C.K.; Khositanont, S.; Chaodumrong, P.; Udchachon, M.; Ekins, S.; Halpin, J. The configuration of Greater Gondwana evidence from LA ICPMS, U Pb geochronology of detrital zircons from the Palaeozoic and Mesozoic of Southeast Asia and China. *Gondwana Res.* **2014**, *26*, 31–51. [CrossRef]

13. Zaw, K.; Meffre, S.; Lai, C.K.; Burrett, C.; Santosh, M.; Graham, I.; Manaka, T.; Salam, A.; Kamvong, T.; Cromie, P. Tectonics and metallogeny of mainland Southeast Asia—A review and contribution. *Gondwana Res.* **2014**, *26*, 5–30.

14. Shi, M.; Zaw, K.; Liu, S.; Xu, B.; Meffre, S.; Cong, F.; Nie, F.; Peng, Z. Geochronology and petrogenesis of Carboniferous and Triassic volcanic rocks in NW Laos: Implications for the tectonic evolution of the Loei Fold Belt. *J. Asian Earth Sci.* **2021**, *208*, 104661. [CrossRef]

15. Hutchison, C.S. Ophiolites in Southeast Asia. *Geol. Soc. Am. Bull.* **1975**, *86*, 797–806. [CrossRef]

16. Hutchison, C.S. *Geological Evolution of South-East Asia*; Geol. Soc. Malaysia; Oxford University Press: Kuala Lumpur, Malaysia, 2007; 406p.

17. Mitchell, A.H.G. Cretaceous-Cenozoic tectonic events in the Western Myammar (Burma)-Assam region. *J. Geol. Soc. Lond.* **1993**, *150*, 1089–1102. [CrossRef]

18. Lee, T.Y.; Lawver, L.A. Cenozoic plate reconstructions of Southeast Asia. *Tectonophysics* **1995**, *251*, 85–138. [CrossRef]

19. Cheng, R.; Uchida, E.; Katayose, K.; Yarimizu, K.; Shin, K.C.; Kong, S.; Nakano, T. Petrogenesis and tectonic setting of Late Paleozoic to Late Mesozoic igneous rocks in Cambodia. *J. Asian Earth Sci.* **2019**, *185*, 104046. [CrossRef]

20. Kasahara, N.; Niki, S.; Uchida, E.; Yarimizu, K.; Cheng, R.; Hirata, T. Zircon U–Pb chronology on plutonic rocks from northeastern Cambodia. *Heliyon* **2021**, *7*, e06752. [CrossRef]

21. Uchida, E.; Nagano, S.; Niki, S.; Yonezu, K.; Saitoh, Y.; Shin, K.C.; Hirata, T. Geochemical and radiogenic isotopic signatures of granitic rocks in Chanthaburi and Chachoengsao provinces, southeastern Thailand: Implications for origin and evolution. *J. Asian Earth Sci. X* **2022**, *8*, 100111. [CrossRef]

22. Hung, D.D.; Tsutsumi, Y.; Hieu, P.T.; Minh, N.T.; Minh, P.; Dung, N.T.; Hung, N.B.; Komatsu, T.; Hoang, N.; Kawaguchi, K. Van Canh Triassic granite in the Kontum Massif, central Vietnam: Geochemistry, geochronology, and tectonic implications. *J. Asain Earth Sci. X* **2022**, *7*, 100075. [CrossRef]

23. Uchida, E.; Yokokura, T. Differences in geochemical characteristics and tectonic settings between Hai Van granitic rocks in Da Nang Province and Van Canh plutonic rocks in Quang Nam Province, Central Vietnam. *Geosciences* **2024**, *14*, 13. [CrossRef]

24. Mantajit, N.; Hintong, C. *Geological map of Thailand: Scale 1: 2,500,000*; Geological Survey Division, Department of Mineral Resources: Bangkok, Thailand, 1999.

25. Jaffey, A.H.; Flynn, K.F.; Glendenin, L.E.; Bentley, W.T.; Essling, A.M. Precision measurement of half-lives and specific activities of $^{235}$U and $^{238}$U. *Phys. Rev.* **1971**, *C4*, 1889–1906.

26. Jochum, K.P.; Brueckner, S.M. Reference materials in geoanalytical and environmental research—Review for 2006 and 2007. *Geostand. Geoanal. Res.* **2008**, *32*, 405–452. [CrossRef]

27. Sakata, S.; Hirakawa, S.; Iwao, H.; Danhara, T.; Guillong, M.; Hirata, T. A new approach for constraining the magnitude of initial disequilibrium in Quaternary zircon by coupled uranium and thorium decay series dating. *Quat. Geochronol.* **2017**, *38*, 1–12. [CrossRef]

28. Jackson, S.E.; Pearson, N.J.; Griffin, W.L.; Belousova, E.A. The application of laser ablation-inductively coupled plasma-mass spectrometry to in situ U-Pb zircon geochronology. *Chem. Geol.* **2004**, *211*, 47–69. [CrossRef]

29. Iwano, H.; Orihashi, Y.; Hirata, T.; Ogasawara, M.; Danhara, T.; Horie, K.; Hasebe, N.; Sueoka, S.; Tamura, A.; Hayasaka, Y.; et al. An inter-laboratory evaluation of OD-3 zircon for use as a secondary U–Pb dating standard. *Island Arc* **2013**, *22*, 382–394. [CrossRef]

30. Vermeesch, P. IsoplotR: A free and open toolbox for geochronology. *Geosci. Front.* **2018**, *9*, 1479–1493. [CrossRef]

31. Ludwig, K.R. On the treatment of concordant uranium-lead ages. *Geochem. Cosmochim. Acta* **1998**, *62*, 665–676. [CrossRef]

32. Tanaka, T.; Togashi, S.; Kamioka, H.; Amakawa, H.; Kagami, H.; Hamamoto, T.; Yuhara, M.; Orihashi, Y.; Yoneda, S.; Shimizu, H. JNdi 1: A neodymium isotopic reference in consistency with LaJolla neodymium. *Chem. Geol.* **2000**, *168*, 279–281. [CrossRef]

33. Faure, G.; Mensing, T.M. *Isotopes—Principles and Applications*, 3rd ed.; John Wiley & Sons: Hoboken, NJ, USA, 2005; pp. 347–411.

34. Uchida, E.; Yonezu, K.; Yokokura, T.; Mori, N. Diffeences in geochemical signatures and petrogenesis between the Van Canh and Ben Giang-Que Son granitic rocks in the southern Kontum Masif, Vietnam. *Geosciences* **2023**, *13*, 341. [CrossRef]

35. Ishihara, S. The magnetite series and ilmenite series granitic rocks. *Min. Geol.* **1977**, *27*, 293–305.

36. Ishihara, S. The Granitoid Series and Mineralization. In *Economic Geology Seventy Fifth Anniversary Volume*; Skinner, B.J., Ed.; Economic Geology Publishing Company: Littleton, CO, USA, 1981; pp. 458–484.
37. Cox, K.G.; Bell, J.D.; Pankhurst, R.J. *The Interpretation of Igneous Rocks*; Allen and Unwin: London, UK, 1979; p. 450.
38. Wilson, M. Igneous Petrogenesis. In *A Global Tectonic Approach*; Unwin Hyman: London, UK, 1989; p. 466.
39. Irvine, T.L.I.; Baragar, W.R.A. A guide to chemical classification of common volcanic rocks. *Can. J. Earth Sci.* **1971**, *8*, 523–548. [CrossRef]
40. Chappell, B.W.; White, A.J.R. Two contrasting granite types. *Pac. Geol.* **1974**, *8*, 173–174.
41. Middlemost, E.A.K. Naming materials in the magma/igneous rock system. *Earth Sci. Rev.* **1994**, *37*, 215–224. [CrossRef]
42. Whalen, J.B.; Currie, K.L.; Chappell, B.W. A-type granites: Geochemical characteristics, discrimination and petrogenesis. *Contrib. Miner. Petrol.* **1987**, *95*, 407–419. [CrossRef]
43. Pearce, J.A.; Harris, N.B.W.; Tindle, A.G. Trace element distribution diagrams for the tectonic interpretation of granitic rocks. *J. Petrol.* **1984**, *25*, 956–983. [CrossRef]
44. Defant, M.J.; Drummond, M.S. A model for Trondhje Tonalite Dacite Genesis and crustal growth via slab melting: Archean to modern comparisons. *J. Geophys. Res. Solid Earth Banner* **1990**, *95*, 21503–21521.
45. McDonough, W.F.; Sun, S.S. The composition of the Earth. *Chem. Geol.* **1995**, *120*, 223–253. [CrossRef]
46. Masuda, A.; Nakamura, N.; Tanaka, T. Fine structures of mutually normalized rare earth patterns of chondrites. *Geochim. Cosmochim. Acta* **1973**, *37*, 239–248. [CrossRef]
47. Schaefer, B.F. *Radiogenic Isotope Geochemistry*; Oxford University Press: Oxford, UK, 2016; pp. 40–56, 145–176.
48. Uchida, E.; Endo, S.; Makino, M. Relationship between solidification depth of granitic rocks and formation of hydrothermal ore deposits. *Resour. Geol.* **2007**, *57*, 47–56. [CrossRef]
49. Uchida, E.; Choi, S.G.; Baba, D.; Wakisaka, Y. Petrogenesis and solidification depth of the Jurassic Daebo and Cretaceous Bulguksa granitic rocks in South Korea. *Resour. Geol.* **2012**, *62*, 281–295. [CrossRef]
50. Mitchell, A.H.G. Guides to metal provinces in the central Himalaya collision belt; the value of regional stratigraphic correlations and tectonic analogies. *Mem. Geol. Soc. China* **1979**, *3*, 167–194.
51. Morley, C.K. Nested strike–slip duplexes and other evidence for late Cretaceous–Palaeogene transpressional tectonics before and during the India-Eurasia collision, in Thailand, Burma and Malaysia. *J. Geol. Soc. Lond.* **2004**, *161*, 799–812. [CrossRef]
52. Mitchell, A.H.G.; Htay, M.T.; Htun, K.M. The medial Myanmar suture zone and the Western Myanmar-Mogok foreland. *J. Myanmar Geosci. Soc.* **2015**, *6*, 73–88.
53. Cobbing, E.J.; Pitfield, P.E.J.; Darbyshire, D.P.F.; Mallick, D.I.J. The Granites of the South-East Asian Tin Belt. Available online: https://webapps.bgs.ac.uk/data/publications/pubs.cfc?method=viewRecord&publnId=19864782&series=OG&subseries=RP (accessed on 9 April 2024).
54. Dunning, G.R.; MacDonald, A.S.; Barr, S.M. Zircon and monazite U-Pb dating of the Doi Inthannon core complex, northern Thailand: Implications for extension within the Indosinian Orogen. *Tectonophysics* **1995**, *251*, 197–213. [CrossRef]